

Investigation on guanidinium bromide incorporation in methylammonium lead iodide for enhanced efficiency and stability of perovskite solar cells

Mano Balaji Gandhi^{a,c}, Arivazhagan Valluvar Oli^a, Stefan Nicholson^{a,b}, Milan Adelt^b, Robert Martin^b, Yu Chen^b, Moorthy Babu Sridharan^{c,*}, Aruna Ivaturi^{a,*}

^a Smart Materials Research and Device Technology Group, Department of Pure and Applied Chemistry, University of Strathclyde, Glasgow G1 1XL, United Kingdom

^b Department of Physics, SUPA, University of Strathclyde, 107 Rottenrow, Glasgow G4 0NG, United Kingdom

^c Crystal Growth Centre, Anna University, Chennai 600025, Tamilnadu, India

ARTICLE INFO

Keywords:

Guanidinium bromide
Compositional engineering
Multiple cation perovskite
Mixed halide perovskite
Surface passivation

ABSTRACT

A guanidinium incorporated double cation mixed halide perovskite was investigated by including guanidinium bromide (GABr) in methylammonium lead iodide (MAPI) under various GABr concentrations. The XRD patterns with characteristic (1 1 0), (2 2 0) and (3 1 0) peaks showed an initial shift towards lower angles and then towards higher angles, indicating an initial lattice expansion and then contraction with increasing GABr content. Increasing the GABr concentration above 10% resulted in reducing the visible absorbance of the compound along with widening of the bandgap. The bandgap increased from 1.58 eV for MAPI to 2.06 eV for 80% GABr but not for 1–10% GABr. Steady state and time resolved photoluminescence measurements revealed that the 10% GABr incorporated samples exhibited higher photoluminescence emission and enhanced charge carrier lifetime than MAPI. The scanning electron microscopy images depicted typical surface passivation effect observed in the GA based additives, where an increase in grain size and low number of pinholes were observed for 10% GABr incorporated films. As an outcome of these synergistic effects, perovskite solar cells (PSCs) fabricated from 10% GABr presented a superior power conversion efficiency (PCE) of $16.70 \pm 0.20\%$ compared to the conventional MAPI (PCE = $15.35 \pm 0.15\%$). The 10% GABr based PSCs exhibited lesser hysteresis compared to MAPI and retained > 97% of their pristine PCE after 400 h of continuous illumination, while the PCE of MAPI-based PSCs deteriorated with time.

1. Introduction

Hybrid perovskite solar cells (PSCs) have accomplished an iconic development in solar cell research in the past decade. They have shown rapid progress with the power conversion efficiencies (PCEs) steeply increasing from 3.8% (Kojima et al., 2009) to 25.7% (Kim et al., 2022) — a stark increase in a span of 13 years which none of the existing thin film solar cell technologies have achieved. The hybrid metal halide perovskites exhibit attractive optoelectronic properties, such as high absorption coefficient (Im et al., 2011), easy bandgap tuneability by compositional engineering (Park, 2014), ambipolar charge carrier mobility (Giorgi and Yamashita, 2015), longer carrier lifetime and diffusion length (Stranks et al., 2013), etc., which make them a favorable material for efficient solar energy harvesting. One of the important reasons allowing PSCs to achieve this unprecedented progress is the ease of tuning the material properties by varying the molecular and/or

elemental composition of the individual sites in the ABX_3 perovskite composition (Jena et al., 2019; Saliba et al., 2018), where *A* is an organic or inorganic cation, *B* is a metal cation and *X* is a halogen anion. The compositional engineering of the perovskite compound has significance in exploring various combinations of materials and eventually lead to the development of new mixed halide, and mixed cation perovskites. These mixed composition perovskites have shown better performance compared to the conventional perovskite compounds (Ganose et al., 2017).

Multiple cation perovskites have attracted a lot of attention in recent years. The incorporation of two or more cations in the *A* site of the perovskite structure results in effective outcomes, such as enhanced structural/phase stability (Koh et al., 2016), reduced defects due to surface passivation, and enhanced device stability compared to the regular perovskite absorber materials (Dong et al., 2019; Stoumpos et al., 2017). A number of cations are feasible (Dong et al., 2019) to be

* Corresponding authors.

E-mail addresses: babu@annauniv.edu (M. Babu Sridharan), aruna.ivaturi@strath.ac.uk (A. Ivaturi).

<https://doi.org/10.1016/j.solener.2023.01.026>

Received 4 September 2022; Received in revised form 6 January 2023; Accepted 12 January 2023

Available online 17 February 2023

0038-092X/© 2023 The Author(s). Published by Elsevier Ltd on behalf of International Solar Energy Society. This is an open access article under the CC BY license (<http://creativecommons.org/licenses/by/4.0/>).

incorporated individually or simultaneously in the perovskite geometry to form the multiple cation configuration. Some of the cations which have been investigated are cesium (Cs) (Choi et al., 2014; Kulbak et al., 2016; Premkumar et al., 2019), rubidium (Rb) (Park et al., 2017; Saliba et al., 2016a), formamidinium [HC(NH₂)₂; FA] (Liao et al., 2016; Suzuki et al., 2021), methylammonium (CH₃NH₃; MA), and guanidinium [C(NH₂)₃; GA] (De Marco et al., 2016; Jodlowski et al., 2017; Saliba et al., 2016b). These cations have been incorporated in double, triple and quadruple configurations, and their physical properties and device characteristics were investigated. The GA cation has attracted considerable interest as an additive in methylammonium lead iodide (CH₃NH₃PbI₃; MAPI), due to its ability to enhance the film quality by passivating the film defects (De Marco et al., 2016; Jodlowski et al., 2017; Yerramilli et al., 2021). GA was basically used as an additive in MAPI to suppress the nonradiative charge recombination at the grain boundaries. The initial research demonstrated that the GA iodide (GAI) additive assists in passivating the film surface resulting in reduced number of grain boundaries leading to longer carrier lifetimes and ultimately enhancing the device parameters (before GA incorporation: $V_{oc} = 1.025$ V; $J_{sc} = 21.27$ mA/cm²; FF = 75%; PCE = 16.35%; after GA incorporation: $V_{oc} = 1.071$ V; $J_{sc} = 21.24$ mA/cm²; FF = 75.31%; PCE = 17.13%) (De Marco et al., 2016). A subsequent research demonstrated that the inclusion of GA cation is not just a surface passivation phenomenon, but direct incorporation of GA occurs when mixed with methylammonium lead iodide. The work proposed that GA being larger in size ($r_{eff} = 278$ pm) compared to MA ($r_{eff} = 217$ pm) (Zhang et al., 2019) occupies the interstitial vacancy between the PbX₆ octahedron framework, which results only in a slight expansion in the unit cell when < 20% is included in methylammonium lead iodide. The fabricated champion PSCs exhibited the following device parameters of $V_{oc} = 1.082$ V; $J_{sc} = 23.19$ mA/cm²; FF = 80.3%; PCE = 20.15% for 14% GA inclusion and $V_{oc} = 1.050$ V; $J_{sc} = 22.50$ mA/cm²; FF = 80%; PCE = 18.88% for MAPI (Jodlowski et al., 2017). The adaptability of the GA incorporation for a different device configuration was also researched, where GA chloride (GACl) was employed as an additive in MAPI for the hole transport layer-free mesoscopic device configuration. The GACl additive resulted in enhanced carrier lifetime and reduced charge carrier loss due to its surface passivation effect. The device parameters of $V_{oc} = 0.88$ V; $J_{sc} = 15.10$ mA/cm²; FF = 68%; PCE = 9.10% were achieved for MAPI, while $V_{oc} = 1.00$ V; $J_{sc} = 19.31$ mA/cm²; FF = 74%; PCE = 14.35% were achieved for the GACl-based hole transport layer-free mesoscopic device configuration (Hou et al., 2017). The above results suggest that the GA cation in MAPI can result in effective enhancement of the quality of the films by surface passivation. A quadruple cation perovskite compound Cs_{0.05}(FA)_{0.83}(MA)_{1-x}(GA)_x(I_{0.83}Br_{0.17})₃ was reported by (Zhang et al., 2019). Maintaining the composition of Cs and FA constant, GA was varied with respect to MA and the corresponding material and device characteristics were investigated. The GA-based devices showed a stabilized PCE of 20.29% ($V_{oc} = 1.12$ V; $J_{sc} = 23.1$ mA/cm²; FF = 78.4%; PCE = 20.29%, and $V_{oc} = 1.08$ V; $J_{sc} = 22.4$ mA/cm²; FF = 76.3%; PCE = 18.45% without GA), the best efficiency for GA doped perovskites under any device configuration. The devices showed better stability owing to the mixed dimensionality (3D CsFA-MA)_{1-x}(GA)_x; 2D FAGAPbI₄; and 1D δ-FAPbI₃) of the individual perovskite compounds. Several other studies have been reported in the literature where the impact of the GA cation on the structural, optical, morphological and device properties of the PSCs were investigated (Giorgi et al., 2015; Ishibashi et al., 2017; Kubicki et al., 2018; Kulkarni et al., 2017; Mahapatra et al., 2020; Vega et al., 2018). Recently, Chavan et al. demonstrated the interfacial modification of cesium–formamidinium lead iodide perovskite by employing GAI salt as an interlayer. This interfacial engineering improved charge transfer at the interfaces and resulted in increasing the PCE from 19.22% to 20.07% (Chavan et al., 2020).

GA bromide (GABr) has been employed as a passivating agent to passivate the defects in perovskite quantum dots (Gong et al., 2021;

Jung et al., 2020). Apart from defect passivation, GABr has been used in wide bandgap perovskite materials (FAPbBr₃, GAsnI₂Br and Cs_(1-x)Rb_xPbI₂Br) to improve crystallization and structural stability (Chen et al., 2021; Xu et al., 2022; Zhang et al., 2020). Thus, we hypothesize that the inclusion of GABr in MAPI might improve the PCE (via defect passivation) and the structural stability of the MAPI-based PSCs, which is the main motivation for choosing GABr in the present study. The majority of literature is focused on GAI and GACl additive incorporation in MAPI, while the impact of GABr in MAPI remains unexplored. To extend the research of GA halide additives in PSCs, the present study explores the impact of GABr as an additive in MAPI. We report a double cation mixed halide perovskite compound methylammonium–guanidinium lead iodo–bromide (referred to as GAMA in the following sections). The effect of GABr concentrations (vol.%) on the structural, optical, morphological and device properties were investigated. The results indicate that GABr is a viable additive in MAPI to improve the device performance and eventually improve the device stability.

2. Structural properties of GABr incorporated MAPI

The X-ray diffraction (XRD) patterns of the double cation mixed halide perovskite compound are shown in Fig. 1(a). The XRD pattern for MAPI shows characteristic peaks of the tetragonal phase at $2\theta = 14.5^\circ$, 28.7° and 32.3° corresponding to the (1 1 0), (2 2 0) and (3 1 0) planes (Almutawah et al., 2018; Manukyan et al., 2016; Zhao and Zhu, 2013). The observed shift of the diffraction peaks toward lower angle (Fig. 1(b)) might be due to the influence of the GA cation. This indicates the expansion of the unit cell due to the larger GA cation (ionic radius = 278 pm) (Jodlowski et al., 2017) substitution for MA cation (ionic radius = 217 pm) (Zhang et al., 2019) in the MAPI lattice. This trend continues until 10% GABr after which the peaks shift toward higher angles, suggesting contraction of the unit cell. This phenomenon can be explained by understanding the substitution process of the A-site cation in the lattice. The formation of a perovskite compound is governed by the Goldschmidt tolerance factor (Goldschmidt, 1926) that determines the ability of a compound to crystallize in the perovskite structure, which is defined by the ratio of ionic radii of the A, B and X site ions given by the following formula (Filip and Giustino, 2018):

$$t = r_A + r_X / \sqrt{2}(r_B + r_X)$$

where r_A , r_B and r_X are the ionic radii of the A, B and X ions. A tolerance factor in the range 0.8–1.0 results in the formation of three-dimensional (3D) cubic perovskite structure. MAPI has a tolerance factor of ~ 0.8 , while GA lead bromide is calculated to be ~ 1.4 . This suggests that pure GA lead bromide crystallizes in lower-dimensional perovskite structure, which possess wide bandgap and usually does not favor light absorber applications. In addition to the tolerance factor, the octahedral factor (μ) is also relevant for the formation of perovskite structure. The octahedral factor (μ) is the ratio between the ionic radii of B and X ions. In our case, when the Γ^- ($r_{avg} \sim 198$ pm) is replaced by the Br⁻ ion ($r_{avg} \sim 185$ pm), which is smaller than Γ^- , it results in an increase of the octahedral factor. However, this also implies that the decrease in the halogen ion size reduces the BX₆ octahedral size accommodating larger GA cation in the MAPI lattice.

When the GABr concentration is increased from 1 to 10%, the larger GA cation can substitute for MA only within a limit governed by the tolerance and octahedral factors. This is evident from the low-angle shift of the XRD peaks suggesting an expansion of the unit cell due to the larger GA cation. We observe that once the GABr concentration crosses a certain limit, formation of GA lead halide secondary phases (GAPbI₃ and GAPbBr₃) occurs, as the MAPI lattice can no longer accommodate the GA cations at such high concentrations. This is supported by the diminishing of the peaks in the 20° – 30° 2θ range. Further increasing the concentration increases the formation of GA lead halide phases. This is

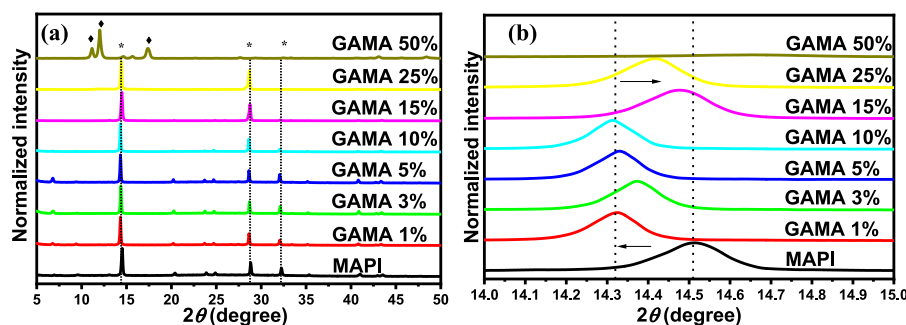


Fig. 1. (a) XRD patterns of MAPI with different GABr concentrations. (b) Enlarged view of the characteristic (1 1 0) peak presenting a shift in the peak position with increasing GABr concentration. ‘♦’ and ‘*’ symbols indicate GA halide and MAPI phases, respectively.

evidenced from the shift of the peaks to the initial position implying a unit cell shrinkage, indicating that the MAPI unit cell is returning to its original form, but it might be over shadowed by the co-existing GA lead halide phases dominating the concentration. The XRD pattern of the 50% GAMA matches with GA lead bromide confirming the formation of complete GA cation based two-dimensional (2D) perovskite.

Additionally, the crystallite size for MAPI and 1–50% GAMA was estimated from the Scherrer equation given as follows:

$$D = \frac{k\lambda}{\beta \cos\theta}$$

where k is the Scherrer constant ($k = 0.94$), λ is the wavelength of the X-ray source (0.15406 nm), β is the full width at half maximum (FWHM) of the diffraction peak and θ is the corresponding diffraction angle ($^{\circ}$). The estimated crystallite size along with the θ and FWHM values are given in Table 1. It can be observed that the FWHM and θ gradually decrease with increase in the GABr concentration up to 10%, which coincides with the XRD pattern in Fig. 1(b). The 50% GABr presents a higher FWHM with the lowest crystallite size. The decrease in the FWHM and the change in crystallite size from 7.64 nm for MAPI to 10.41 nm for 10% GABr suggest that crystallite size in the film increases for the lower concentrations of GABr. The XRD analysis confirms the successful incorporation of GABr into the MAPI lattice.

3. Impact of GABr on the optical properties of MAPI

The UV–visible (UV–Vis) absorbance of GABr incorporated double cation mixed halide perovskite is given in Fig. 2(a). The influence of GABr in MAPI can be observed by the enhancement of the absorbance for 3% GABr. However, this was not the trend for the remainder of the concentration since the absorbance decreases with further increasing in GABr concentration. As observed in the XRD results, increasing the GABr concentration to higher values results in the formation of GA lead halide secondary phases which is evidenced by two new peaks at 530 and 580 nm (Kulkarni et al., 2017), and the disappearance of the characteristic 780 nm peak for 80% GABr. The bandgaps of the compounds derived from the absorbance spectra (Fig. S1) indicate that the bandgap increases with increasing GABr content (Fig. 2(b)). The bandgap increased from 1.581 eV for MAPI to 2.059 eV for 80% GABr. However, the bandgap remains almost unaltered for lower concentrations [bandgaps

Table 1

The average crystallite sizes of MAPI and 1–50% GAMA perovskite.

GABr (%)	FWHM	θ ($^{\circ}$)	D (nm)
MAPI	0.1911	14.50	7.64
1	0.1459	14.31	9.92
3	0.1475	14.36	9.89
5	0.1388	14.32	10.51
10	0.1402	14.31	10.41
50	0.3245	12.02	4.49

of 1.592, 1.591, 1.594 and 1.594 eV, respectively, for 1, 3, 5 and 10% GABr]. Also, the absorbance remains fairly unchanged suggesting that lower concentrations of GABr does not alter the optical absorption properties. The widening of the bandgap for higher concentrations can be ascribed to the formation of hybrid lead bromide perovskites, which usually possess wider bandgap ($\text{CH}_3\text{NH}_3\text{PbBr}_3 = 2.3$ eV; $\text{CH}_3\text{NH}_3\text{Pb}(\text{I}_{1-x}\text{Br}_x)_3 = 1.60\text{--}2.33$ eV; $\text{GAPbBr}_3 = 2.52$ eV) (Park et al., 2015; Sheng et al., 2015). These results support the co-existence of the different perovskite phases which was observed from the XRD results. The UV–Vis analysis, however, indicates that inclusion of smaller quantities of GABr in MAPI will marginally widen the bandgap but retain the characteristic broad absorbance in the visible region.

The steady-state photoluminescence (PL) emission spectra of MAPI and 1, 3, 5 and 10% GABr incorporated samples shown in Fig. 2(c) reveal a similar trend as observed in the absorption spectra. All the samples show identical band to band emission peak position, however, the intensity drastically drops for 1, 3 and 5% and then increases for 10%. The 10% GABr shows the relatively better emission compared to MAPI. This decrease and increase in the PL emission intensity can be ascribed to the characteristic passivation effect of the GA cation (De Marco et al., 2016; Hou et al., 2017; Yerramilli et al., 2021). The 3% GABr concentration (which exhibited higher absorption in the UV–Vis absorption spectra) shows a lower PL emission which can be ascribed to the intrinsic segregation of elemental halogen ions (Gratia et al., 2016). When we increase the GABr concentration in MAPI, the Br^- content is simultaneously increased in the perovskite which has the ability to diffuse and segregate as individual halide ions and interfere with characteristic absorption spectra, resulting in an increase in the absorbance for 3% GABr (Fang et al., 2021; Fu et al., 2021). This intrinsic halogen segregation is a random process and this might be a reason for the difference between the UV–Vis absorption and PL emission spectra. The enhanced emission might be due to the passivation effect of the GA cations as a result of decreased the surface defects and increased the grain size, which in turn reduces the charge recombination at the grain boundaries. Time-resolved PL (TRPL) measurements were performed on 10% GAMA to evaluate the charge carrier lifetime, and were compared with MAPI (the measurement was performed on perovskite films coated on glass substrates). The TRPL measurement [Fig. 2(d) and (e)] revealed the carrier lifetime of 10% GAMA (380.80 ± 2.4 ns) to be higher than MAPI (276.78 ± 0.5 ns) (Kim et al., 2019). The optical and structural properties of GABr incorporated double cation mixed halide perovskite indicates that GABr concentration of 10% or less is desirable for fabrication of PSCs. Higher concentrations result in the formation of GA based two-dimensional perovskite phases which do not possess favorable optoelectronic properties (Kulkarni et al., 2017).

4. J–V characteristics of GABr incorporated MAPI

The SEM analysis was performed on the perovskite samples coated on FTO/SnO₂ substrate. Surface micrographs of MAPI, 1, 3 and 10%

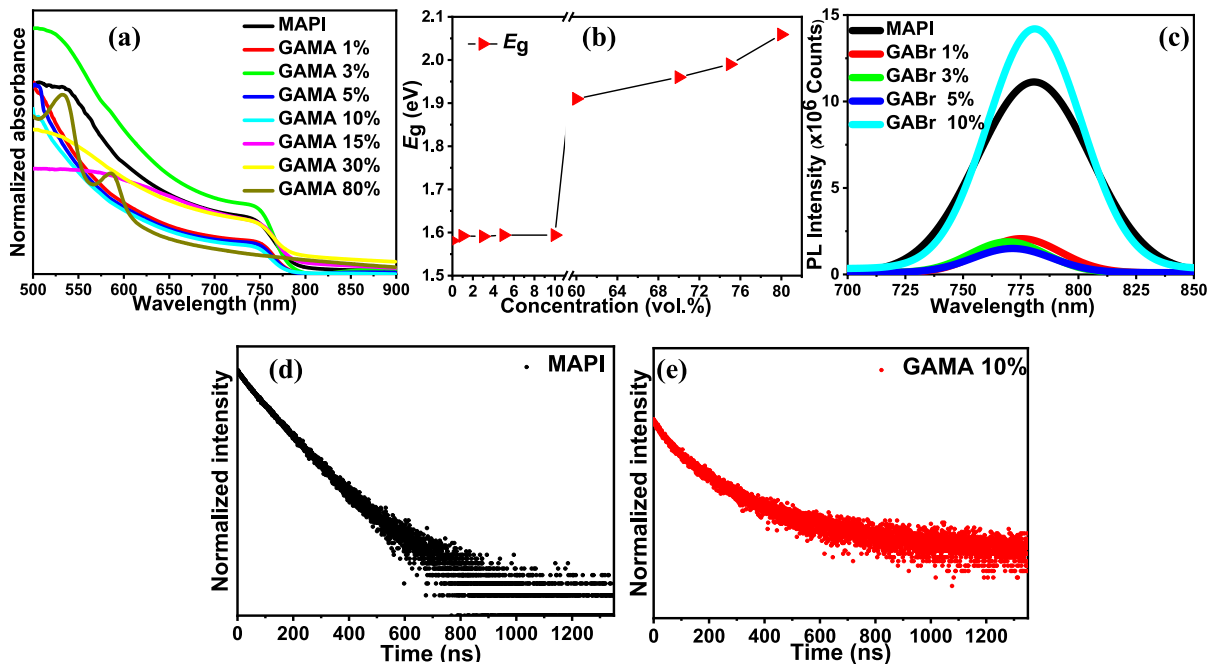


Fig. 2. (a) UV-Vis absorbance spectra of MAPI films with different GABr concentrations (coated with protective PMMA) deposited on glass. (b) Calculated E_g for different GABr concentrations showing an increasing trend for higher GABr concentration. (c) Steady state PL emission spectra showing enhanced emission for 10% GABr. TRPL curves of (d) MAPI and (e) GAMA 10% showing enhanced carrier lifetime for GAMA 10%.

GABr incorporated MAPI thin films are shown in Fig. 3(a)–(d). The scanning electron micrograph of the MAPI film show smaller grain size and a large number of pinholes, whereas the GABr included MAPI films shows a planar surface with larger grains and low number of pinholes. The 10% GABr film shows the largest grain size with smallest number of pinholes compared to MAPI. PSCs were fabricated in n-i-p configuration with FTO/SnO₂/Perovskite/Spiro-OMeTAD/Ag device architecture (Fig. S2). The thickness of the SnO₂, perovskite and spiro-OMeTAD layers is found to be 110, 750 and 250 nm, respectively. GABr concentrations of 1, 3, 5 and 10% were chosen for PSC fabrication based on the structural and optical results and their performance was compared with conventional MAPI-based PSC. The $J-V$ curves (reverse scan) of the solar cells are shown in Fig. 3(e) and their photovoltaic parameters are

Table 2

Photovoltaic parameters of the PSCs fabricated with different GABr concentrations. The errors were calculated by finding the standard deviation (SD) for 10 values (including champion) and the derived SD value was used to estimate the standard error.

GABr (%)	V_{oc} (V)	J_{sc} (mA/cm ²)	FF (%)	PCE (%)
MAPI	1.06 ± 0.01	20.25 ± 0.19	71.3 ± 0.50	15.35 ± 0.15
1	1.05 ± 0.01	17.49 ± 0.14	71.9 ± 0.60	13.25 ± 0.13
3	1.03 ± 0.02	20.14 ± 0.12	74.2 ± 0.40	15.54 ± 0.19
5	1.01 ± 0.01	21.48 ± 0.12	73.5 ± 0.70	15.97 ± 0.14
10	1.01 ± 0.01	22.21 ± 0.17	73.8 ± 0.50	16.70 ± 0.2

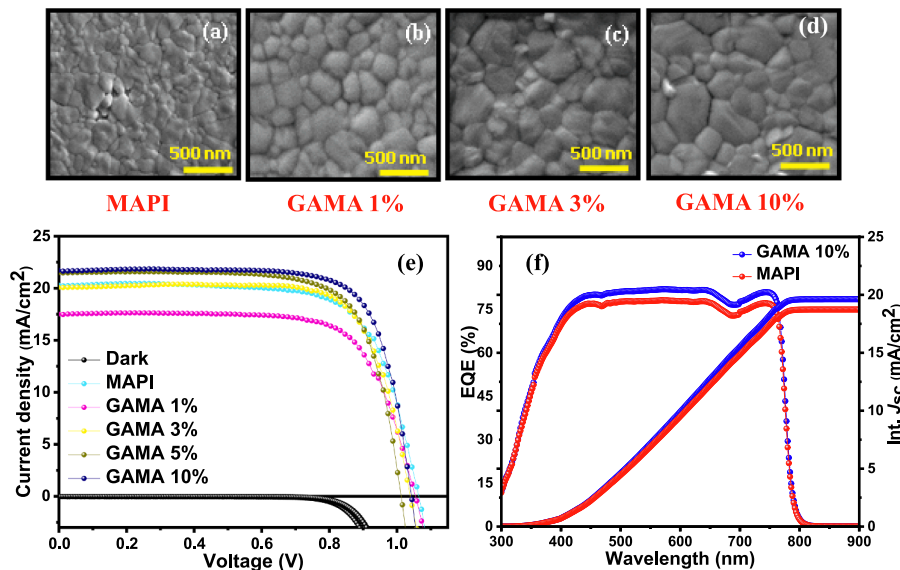


Fig. 3. (a)–(d) SEM images of MAPI, 1, 3 and 10% GAMA films. (e) $J-V$ curves (reverse scan) of PSCs fabricated from 1, 3, and 10% GABr. 10% GABr PSCs show superior performance compared to MAPI. (f) EQE spectra of MAPI compared with GABr 10%, where 10% GABr included MAPI shows higher EQE.

tabulated in Table 2. The MAPI-based PSCs exhibited average device parameters of $V_{oc} = 1.06$ V, $J_{sc} = 25.25$ mA/cm², FF = 71.30% and PCE = $15.35 \pm 0.30\%$. The PCE decreased to $13.25 \pm 0.50\%$ for 1% GABr, and then increased to $15.54 \pm 0.30\%$ for 3% GABr, $15.97 \pm 0.10\%$ for 5% GABr and finally reached the highest PCE of $16.70 \pm 0.20\%$ for 10% GABr. The variations in the PCE can be ascribed to the obvious change in the film surface morphology due to the inclusion of GABr. The enhanced grain size results in reducing the grain boundaries, which act as trap sites to promote electron–hole recombination. This was realized in the TRPL measurements where an extended carrier lifetime was achieved for 10% GABr and is supported by the increase in the J_{sc} and FF which is an indication of enhanced film quality. The 10% GABr exhibited superior external quantum efficiency (EQE) [Fig. 3(f)] compared to MAPI, which is due to the enhanced film quality as observed in the SEM micrographs. The integrated J_{sc} obtained from the EQE spectra were found to be 19.81 mA/cm² for 10% GABr and 18.86 mA/cm² for MAPI. The mismatch between the J_{sc} values from the J – V curves and EQE spectra can be ascribed to various reasons discussed elsewhere (Saliba and Etgar, 2020). These results reveal that the incorporation of GABr into MAPI to form a double cation mixed halide perovskite compound will be beneficial in improving the device performance of the PSCs.

The consistency of the obtained device parameters for the reverse scan is given in Fig. 4 (box plots for the device parameters under forward scan are given in Fig. S3). It can be observed that the V_{oc} reduces for the increasing GABr concentration. The decrease in the V_{oc} for increasing GABr concentrations can be ascribed to the non-radiative voltage loss induced by the mobile Br[−] ions, which is dominant in perovskite compositions containing high Br[−] (Ebadi et al., 2021). However, a simultaneous increase in the J_{sc} and FF can be noted for the GABr included MAPI-based PSCs. The enhancement of the J_{sc} and FF can be ascribed to the improved film morphology and grain size due the passivation effect of the GA cation. This increase in the J_{sc} and FF also correlates with enhanced EQE observed in the IPCE spectra. The enhancement in the J_{sc} and FF is found to be highest for the GAMA 10%-based PSCs, which might be the reason for the overall increase in the PCE. Thus, it can be summarized that the incorporation of low concentrations of GABr in MAPI can be effective in improving the PCE of MAPI-based PSCs.

The forward and reverse scan J – V plots of MAPI and champion 10% GABr included MAPI are presented in Fig. 5. The presence of hysteresis

in a PSC indicates poor extraction and transfer of the charge carriers to the external circuit. The extraction and transfer of the photo-generated charge carriers can be ascribed to the perovskite film morphology and topography, which influence the charge recombination within the perovskite absorber layer and the heterojunction interface in the PSCs. The forward and reverse scan J – V curve of MAPI (Fig. 5(a)) shows large hysteresis while the champion 10% GABr included MAPI exhibited lower J – V hysteresis. The hysteresis index (HI) of the devices were calculated using the formula.

$$HI = \frac{PCE_{reverse} - PCE_{forward}}{PCE_{reverse}} \times 100.$$

The HI of 10% GABr-based PSCs was calculated to be 8%, which was lesser than the conventional MAPI-based PSC (HI = 14%) (Habisreutinger et al., 2018). The large hysteresis and HI in MAPI might be due to the relatively smaller grain size and pin holes as observed in the SEM micrographs of MAPI (Fig. 3(a)) resulting in poor charge transfer. The improved grain size of 10% GABr-based perovskite film leads to lower charge recombination within the perovskite film (as observed in the TRPL decay curve (Fig. 2(d)), and the enhanced EQE and J_{sc} obtained from the IPCE spectra imply smoother extraction of the charge carriers in the 10% GABr included MAPI based PSC. Thus, it can be concluded that the improved film quality of 10% GABr-based perovskite film contributes to reduced hysteresis.

The stability of the fabricated MAPI and the champion 10% GABr included MAPI-based PSCs was measured under continuous 1 Sun illumination [at ambient conditions in Chennai (RH = 60–65% and room temperature = 34–36 °C)]. The devices were not covered with any encapsulant and PCE was measured at regular intervals under continuous illumination. The stability curves (Fig. 6) show that the 10% GABr-based PSCs exhibit enhanced stability compared to the conventional MAPI. It is observed that the PCE (Fig. 6) remained fairly consistent under continuous illumination (400 h) for the 10% GABr-based PSCs (the stability of the V_{oc} , J_{sc} and FF are given in Fig. S4). The PCE of the 10% GABr included MAPI-based PSC retained > 97% of its pristine PCE after 400 h under continuous illumination ($PCE_{pristine} = 16.70\%$; $PCE_{400\text{ h}} = \sim 16.51\%$), while the PCE of conventional MAPI-based PSC significantly dropped with illumination ($PCE_{pristine} = 15.35\%$; $PCE_{400\text{ h}} = \sim 12.54\%$).

The defects at the grain boundaries in the perovskite films trap the

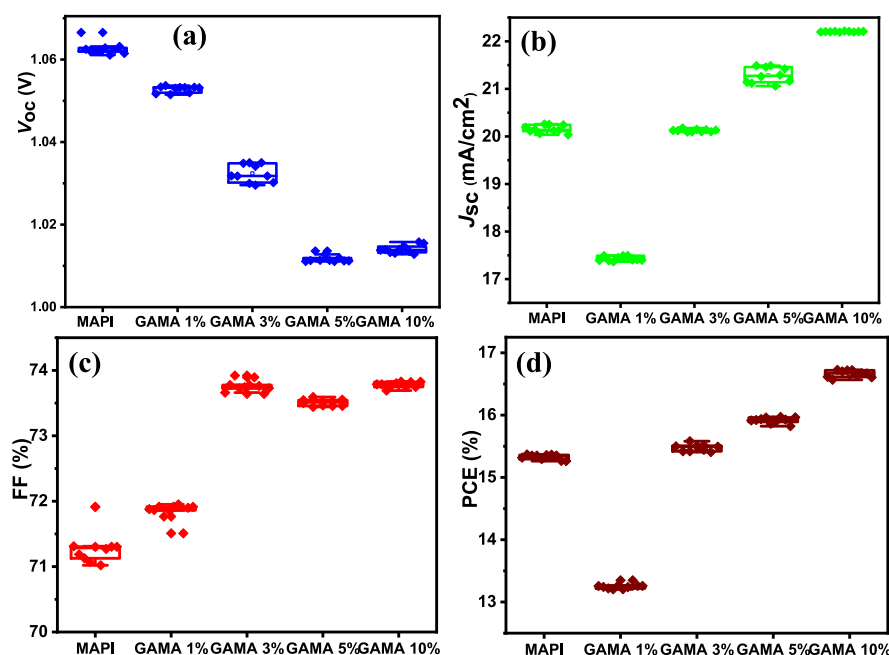


Fig. 4. Box plots of (a) V_{oc} , (b) J_{sc} , (c) FF and (d) PCE of the fabricated MAPI and 1–10% GAMA-based PSCs under reverse scan.

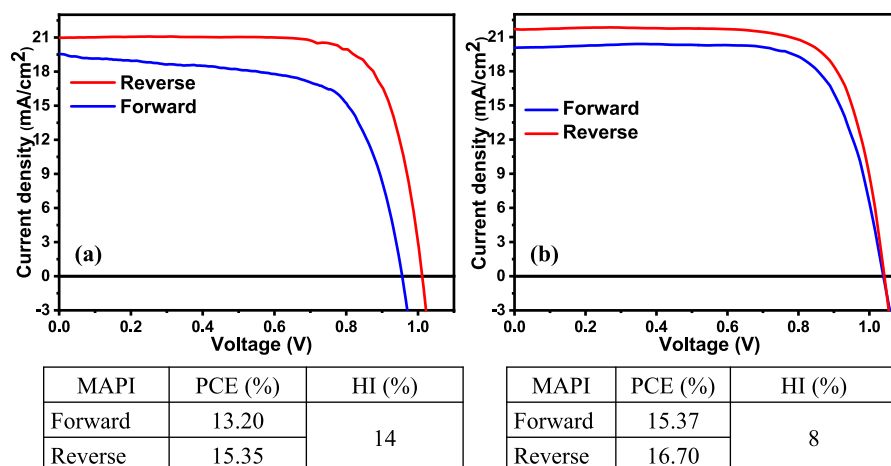


Fig. 5. Forward and reverse scans J - V curves of (a) MAPI and (b) the champion 10% GABr included MAPI-based PSC.

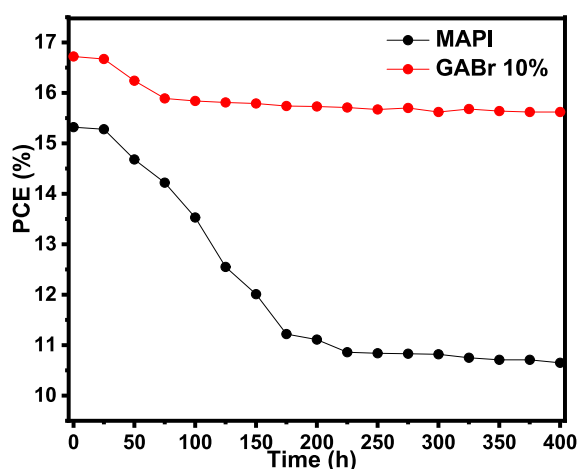


Fig. 6. Stability of MAPI and 10% GABr included MAPI under continuous 1 sun illumination.

photogenerated charge carriers, which promotes non-radiative recombination. The film quality of the perovskite absorber layer is significantly enhanced for 10% GABr inclusion, resulting in increased grain size. Increasing the grain size in the perovskite film implies reduced number of grain boundaries. This decreases the charge carrier

recombination leading to increased photocurrent which is evident from the J - V curve and IPCE spectra [Fig. 3(e) and (f)]. The 10% GABr (with improved film quality compared to MAPI) shows enhanced device stability, due to the reduced photogenerated charge carrier loss, resulting in less non-radiative recombination, eventually reducing the deterioration of the perovskite film. Thus, it is summarized that the incorporation of GABr in MAPI can improve PCE and stability of the PSCs due to the enhanced film morphology obtained by the passivation effect of the GA cation.

Photovoltaic parameters and stability of the 10% GABr included MAPI are compared with the existing GA cation-based PSCs reported in literature and presented in Table 3. The comparison elucidates that the 10% GABr included MAPI shows good stability similar to the existing reports on GA cation-based PSCs. It is noteworthy that the stability of the 10% GABr-based PSCs were studied under elevated operating conditions (RH = 60–65% and 34–36 °C) compared to the existing reports (Table 3). The PCE is, however, lower than the existing reports, which can be ascribed to the different device configuration. Thus, it can be summarized that the GABr inclusion in MAPI significantly improves the stability of the PSCs.

5. Conclusion

In summary, a double cation mixed halide perovskite compound was successfully fabricated by incorporation of GABr into MAPI and the impact of various GABr concentrations was analyzed. The main findings of this work are tabulated in Table S1. A systematic expansion and

Table 3

Comparison of the photovoltaic parameters and stability of 10% GABr-based PSCs with the previously reported GA cations based PSCs.

Perovskite	GA inclusion	Device configuration	PCE (%)		Stability	Experimental conditions	Ref.
			Without GA	With GA			
MAPI	GAI and GACl	ITO/TiO ₂ /Perovskite/spiro-OMeTAD/Au	16.35	17.13	180 h	The devices were stored under dry oxygen atmosphere	(De Marco et al., 2016)
MAPI	GAI	FTO/c-TiO ₂ /mp-TiO ₂ /Perovskite/spiro-OMeTAD/Au	18.88	20.15	1000 h	Under AM1.5G illumination at maximum power point (MPP) tracking (60 °C under Ar atmosphere)	(Jodlowski et al., 2017)
MAPI	GACl	FTO/c-TiO ₂ /mp-TiO ₂ /ZrO ₂ /Carbon/Perovskite ^a	9.10	14.35	—	—	(Hou et al., 2017)
CsFAMA _{1-x} GA _x ^b	GAI	FTO/SnO ₂ /Perovskite/spiro-OMeTAD/Au	18.45	20.29	60 days	The bare devices were exposed at 25 °C and 25% humidity	(Zhang et al., 2019)
MAPI	GABr	FTO/SnO ₂ /Perovskite/spiro-OMeTAD/Ag	15.35	16.70	400 h	Under continuous 1 sun illumination at ambient conditions (RH = 60–65% and 34–36 °C)	This work

^a The PSC was fabricated in a mesoscopic configuration where the MAPI was infiltrated into the TiO₂/ZrO₂/Carbon scaffold.

^b Cs_{0.05}(FA_{0.83}(MA_{1-x}GA_x)_{0.17})_{0.95}Pb(I_{0.83}Br_{0.17})₃, x = 0 to 1.

shrinking of the MAPI unit cell with increase in GABr concentration was observed from the XRD measurements. The lower angle shift of the diffraction peaks indicated the expansion of the unit cell due to the larger GA cation substitution for MA cation in the MAPI lattice. This trend continued until 10% GABr after which the peaks shift toward higher angles, suggesting contraction of the unit cell. The diffraction patterns also revealed that the MAPI and GA lead halide phases co-exist for lower concentrations of GABr. The optical absorbance spectra suggested that the absorbance nonlinearly increases and then decreases as the GABr concentration is increased. The intrinsic segregation of the halogen ions might be the reason for the nonlinear decrease and increase in the absorption and emission spectra. A similar trend is also observed in the steady-state PL emission spectra for the 1% GABr film, which shows less absorption than MAPI. Thus, the authors speculate that this nonlinear change in the emission spectra might be due to the intrinsic halogen ion (Br^- and I^-) segregation. The steady state PL suggested that 10% GABr had a better emission compared to MAPI and the PL decay measurement for 10% GABr showed increased carrier lifetime of 380.80 ± 2.4 ns compared to 276.78 ± 0.5 ns for MAPI. The PSCs fabricated using 10% GABr exhibited enhanced average PCE of $16.70 \pm 0.20\%$ which is higher than the $15.35 \pm 0.15\%$ observed for MAPI. The increase in PCE is due to the enhanced J_{sc} and FF, which is ascribed to the improved film quality as observed in the SEM. The forward and reverse scan $J-V$ plots indicated that the 10% GABr included MAPI showed lesser hysteresis and HI compared to MAPI. The 10% GABr-based PSCs showed better stability by retaining $> 97\%$ of its pristine PCE under 400 h continuous illumination, while the PCE of conventional MAPI deteriorated with time. The increased grain size reduced the number of grain boundaries, which decreases the non-radiative recombination of the charge carriers in the absorber layer. Thus, the reduced radiative recombination in the 10% GABr, eventually, prevents the deterioration of the perovskite film, resulting in improved stability. Based on the presented results, it is proposed that low concentrations of GABr in MAPI can be beneficial in improving the film quality, ultimately resulting in an enhanced device performance.

Declaration of Competing Interest

The authors declare that they have no known competing financial interests or personal relationships that could have appeared to influence the work reported in this paper.

Acknowledgments

We would like to greatly acknowledge Commonwealth Scholarship Commission for funding this research under Commonwealth Split-Site PhD scholarship (2019–2020) for Mano Balaji Gandhi. Aruna Ivaturi would like to acknowledge UK Research and Innovation (UKRI), Engineering and Physical Sciences Research Council (EPSRC) for the Fellowship grant (EP/P011500/1). Moorthy Babu Sridharan sincerely thanks the Defense Research and Development Organisation (DRDO), Ministry of Defense, Government of India (ERIP/ER/201808007/M/01/1740).

Appendix A. Supplementary material

Supplementary data to this article can be found online at <https://doi.org/10.1016/j.solener.2023.01.026>.

References

Almutawah, Z.S., Wathage, S.C., Song, Z., Ahangharnejhad, R.H., Subedi, K.K., Shrestha, N., Phillips, A.B., Yan, Y., Ellingson, R.J., Heben, M.J., 2018. Enhanced grain size and crystallinity in $\text{CH}_3\text{NH}_3\text{PbI}_3$ perovskite films by metal additives to the single-step solution fabrication process. *MRS Adv.* 3 (55), 3237–3242.

Chavan, R.D., Prochowicz, D., Tavakoli, M.M., Yadav, P., Hong, C.K., 2020. Surface treatment of perovskite layer with guanidinium iodide leads to enhanced moisture

stability and improved efficiency of perovskite solar cells. *Adv. Mater. Interfaces* 7 (14), 2000105.

Chen, M., Kamarudin, M.A., Baranwal, A.K., Kapil, G., Ripolles, T.S., Nishimura, K., Hirotsami, D., Sahamir, S.R., Zhang, Z., Ding, C., Sanehira, Y., Bisquert, J., Shen, Q., Hayase, S., 2021. High-efficiency lead-free wide band gap perovskite solar cells via guanidinium bromide incorporation. *ACS Appl. Energy Mater.* 4 (6), 5615–5624.

Choi, H., Jeong, J., Kim, H.-B., Kim, S., Walker, B., Kim, G.-H., Kim, J.Y., 2014. Cesium-doped methylammonium lead iodide perovskite light absorber for hybrid solar cells. *Nano Energy* 7, 80–85.

De Marco, N., Zhou, H., Chen, Q., Sun, P., Liu, Z., Meng, L., Yao, E.-P., Liu, Y., Schiffer, A., Yang, Y., 2016. Guanidinium: a route to enhanced carrier lifetime and open-circuit voltage in hybrid perovskite solar cells. *Nano Lett.* 16 (2), 1009–1016.

Dong, C., Wang, Z.-K., Liao, L.-S., 2019. Progress of triple cation organometal halide perovskite solar cells. *Energ. Technol.* 1900804.

Ebadi, F., Yang, B., Kim, Y., Mohammadpour, R., Taghavinia, N., Hagfeldt, A., Tress, W., 2021. When photoluminescence, electrochromism, and open-circuit voltage diverge – light soaking and halide segregation in perovskite solar cells. *J. Mater. Chem. A* 9 (24), 13967–13978.

Fang, S., Yao, W., Hu, Z., Huang, L., Liu, X., Zhang, H., Zhang, J., Zhu, Y., 2021. Stability in photoinduced instability in mixed-halide perovskite materials and solar cells. *J. Phys. Chem. C* 125 (39), 21370–21380.

Filip, M.R., Giustino, F., 2018. The geometric blueprint of perovskites. *Proc. Natl. Acad. Sci.* 115 (21), 5397.

Fu, S., Xiao, Y., Yu, X., Xiang, T., Long, F., Xiao, J., Ku, Z., Zhong, J., Li, W., Huang, F., Peng, Y., Cheng, Y., 2021. Bandgap adjustment assisted preparation of $>18\%$ $\text{Cs}_3\text{FA}_{1-y}\text{PbI}_3\text{Br}_{3-y}$ -based perovskite solar cells using a hybrid spraying process. *RSC Adv.* 11 (29), 17595–17602.

Ganose, A.M., Savory, C.N., Scanlon, D.O., 2017. Beyond methylammonium lead iodide: prospects for the emergent field of ns^2 containing solar absorbers. *Chem. Commun.* 53 (1), 20–44.

Giorgi, G., Fujisawa, J.-I., Segawa, H., Yamashita, K., 2015. Organic-inorganic hybrid lead iodide perovskite featuring zero dipole moment guanidinium cations: a theoretical analysis. *J. Phys. Chem. C* 119 (9), 4694–4701.

Giorgi, G., Yamashita, K., 2015. Organic-inorganic halide perovskites: an ambipolar class of materials with enhanced photovoltaic performances. *J. Mater. Chem. A* 3 (17), 8981–8991.

Goldschmidt, V.M. 1926. Die Gesetze der Krystallochemie. *Naturwissenschaften* 14 (21), 477–485.

Gong, C., Wang, X., Xia, X., Yang, X., Wang, L., Li, F., 2021. In-situ guanidinium bromide passivation treatment of CsPbBr_3 perovskite quantum dots exhibiting high photoluminescence and environmental stability. *Appl. Surf. Sci.* 559, 149986.

Gratia, P., Grancini, G., Audinot, J.-N., Jeanbourquin, X., Mosconi, E., Zimmermann, I., Dowsett, D., Lee, Y., Grätzel, M., De Angelis, F., Sivula, K., Wirtz, T., Nazeeruddin, M.K., 2016. Intrinsic halide segregation at nanometer scale determines the high efficiency of mixed cation/mixed halide perovskite solar cells. *J. Am. Chem. Soc.* 138 (49), 15821–15824.

Habisreutinger, S.N., Noel, N.K., Saith, H.J., 2018. Hysteresis index: a figure without merit for quantifying hysteresis in perovskite solar cells. *ACS Energy Lett.* 3 (10), 2472–2476.

Hou, X., Hu, Y., Liu, H., Mei, A., Li, X., Duan, M., Zhang, G., Rong, Y., Han, H., 2017. Effect of guanidinium on mesoscopic perovskite solar cells. *J. Mater. Chem. A* 5 (1), 73–78.

Im, J.-H., Lee, C.-R., Lee, J.-W., Park, S.-W., Park, N.-G., 2011. 6.5% efficient perovskite quantum-dot-sensitized solar cell. *Nanoscale* 3 (10), 4088–4093.

Ishibashi, H., Katayama, M., Tanaka, S., Kaji, T., 2017. Hybrid perovskite solar cells fabricated from guanidine hydroiodide and tin iodide. *Sci. Rep.* 7 (1), 4969.

Jena, A.K., Kulkarni, A., Miyasaka, T., 2019. Halide perovskite photovoltaics: background, status, and future prospects. *Chem. Rev.* 119 (5), 3036–3103.

Jodlowski, A.D., Roldán-Carmona, C., Grancini, G., Salado, M., Ralajarisoa, M., Ahmad, S., Koch, N., Camacho, L., de Miguel, G., Nazeeruddin, M.K., 2017. Large guanidinium cation mixed with methylammonium in lead iodide perovskites for 19% efficient solar cells. *Nat. Energy* 2 (12), 972–979.

Jung, K., Choi, H., Kim, H., Chang Park, Y., Lee, M.-J., 2020. Highly luminescent and stable $\text{CH}_3\text{NH}_3\text{PbBr}_3$ quantum dots with 91.7% photoluminescence quantum yield: role of guanidinium bromide dopants. *J. Alloy. Compd.* 832, 154990.

Kim, M., Jeong, J., Lu, H., Lee Tae, K., Eickemeyer Felix, T., Liu, Y., Choi In, W., Choi Seung, J., Jo, Y., Kim, H.-B., Mo, S.-I., Kim, Y.-K., Lee, H., An Na, G., Cho, S., Tress Wolfgang, R., Zakeeruddin Shaik, M., Hagfeldt, A., Kim Jin, Y., Grätzel, M., Kim Dong, S., 2022. Conformal quantum dot-SnO₂ layers as electron transporters for efficient perovskite solar cells. *Science* 375 (6578), 302–306.

Kim, M., Kim, G.-H., Lee, T.K., Choi, I.W., Choi, H.W., Jo, Y., Yoon, Y.J., Kim, J.W., Lee, J., Huh, D., Lee, H., Kwak, S.K., Kim, J.Y., Kim, D.S., 2019. Methylammonium chloride induces intermediate phase stabilization for efficient perovskite solar cells. *Joule* 3 (9), 2179–2192.

Koh, T.M., Thirumal, K., Soo, H.S., Mathews, N., 2016. Multidimensional perovskites: a mixed cation approach towards ambient stable and tunable perovskite photovoltaics. *ChemSusChem* 9 (18), 2541–2558.

Kojima, A., Teshima, K., Shirai, Y., Miyasaka, T., 2009. Organometal halide perovskites as visible-light sensitizers for photovoltaic cells. *J. Am. Chem. Soc.* 131 (17), 6050–6051.

Kubicki, D.J., Prochowicz, D., Hofstetter, A., Sasaki, M., Yadav, P., Bi, D., Pellet, N., Lewński, J., Zakeeruddin, S.M., Grätzel, M., Emsley, L., 2018. Formation of stable mixed guanidinium-methylammonium phases with exceptionally long carrier lifetimes for high-efficiency lead iodide-based perovskite photovoltaics. *J. Am. Chem. Soc.* 140 (9), 3345–3351.

- Kulbak, M., Gupta, S., Kedem, N., Levine, I., Bendikov, T., Hodes, G., Cahen, D., 2016. Cesium enhances long-term stability of lead bromide perovskite-based solar cells. *J. Phys. Chem. Lett.* 7 (1), 167–172.
- Kulkarni, S.A., Baikie, T., Muduli, S., Potter, R., Chen, S., Yanan, F., Bishop, P., Lim, S.S., Sum, T.C., Mathews, N., White, T.J., 2017. Investigating the feasibility of symmetric guanidinium based plumbate perovskites in prototype solar cell devices. *Jpn. J. Appl. Phys.* 56 (8S2), 08MC05.
- Liao, W., Zhao, D., Yu, Y., Shrestha, N., Ghimire, K., Grice, C.R., Wang, C., Xiao, Y., Cimaroli, A.J., Ellingson, R.J., Podraza, N.J., Zhu, K., Xiong, R.-G., Yan, Y., 2016. Fabrication of efficient low-bandgap perovskite solar cells by combining formamidinium tin iodide with methylammonium lead iodide. *J. Am. Chem. Soc.* 138 (38), 12360–12363.
- Mahapatra, A., Runjhun, R., Nawrocki, J., Lewiński, J., Kalam, A., Kumar, P., Trivedi, S., Tavakoli, M.M., Prochowicz, D., Yadav, P., 2020. Elucidation of the role of guanidinium incorporation in single-crystalline MAPbI₃ perovskite on ion migration and activation energy. *PCCP* 22 (20), 11467–11473.
- Manukyan, K.V., Yeghishyan, A.V., Moskovskikh, D.O., Kapaldo, J., Mintairov, A., Mukasyan, A.S., 2016. Mechanochemical synthesis of methylammonium lead iodide perovskite. *J. Mater. Sci.* 51 (19), 9123–9130.
- Park, B.-W., Philippe, B., Jain, S.M., Zhang, X., Edvinsson, T., Rensmo, H., Zietz, B., Boschloo, G., 2015. Chemical engineering of methylammonium lead iodide/bromide perovskites: tuning of opto-electronic properties and photovoltaic performance. *J. Mater. Chem. A* 3 (43), 21760–21771.
- Park, I.J., Seo, S., Park, M.A., Lee, S., Kim, D.H., Zhu, K., Shin, H., Kim, J.Y., 2017. Effect of rubidium incorporation on the structural, electrical, and photovoltaic properties of methylammonium lead iodide-based perovskite solar cells. *ACS Appl. Mater. Interfaces* 9 (48), 41898–41905.
- Park, N.-G., 2014. *Advanced Concepts in Photovoltaics*. The Royal Society of Chemistry, pp. 242–257.
- Premkumar, S., Kundu, K., Umapathy, S., 2019. Impact of cesium in methylammonium lead bromide perovskites: insights into the microstructures, stability and photophysical properties. *Nanoscale* 11 (21), 10292–10305.
- Saliba, M., Correa-Baena, J.-P., Grätzel, M., Hagfeldt, A., Abate, A., 2018. Perovskite solar cells: from the atomic level to film quality and device performance. *Angew. Chem. Int. Ed.* 57 (10), 2554–2569.
- Saliba, M., Etgar, L., 2020. Current density mismatch in perovskite solar cells. *ACS Energy Lett.* 5 (9), 2886–2888.
- Saliba, M., Matsui, T., Domanski, K., Seo, J.-Y., Ummadisingu, A., Zakeeruddin, S.M., Correa-Baena, J.-P., Tress, W.R., Abate, A., Hagfeldt, A., Grätzel, M., 2016a. Incorporation of rubidium cations into perovskite solar cells improves photovoltaic performance. *Science* 354 (6309), 206–209.
- Saliba, M., Matsui, T., Seo, J.-Y., Domanski, K., Correa-Baena, J.-P., Nazeeruddin, M.K., Zakeeruddin, S.M., Tress, W., Abate, A., Hagfeldt, A., Grätzel, M., 2016b. Cesium-containing triple cation perovskite solar cells: improved stability, reproducibility and high efficiency. *Energ. Environ. Sci.* 9 (6), 1989–1997.
- Sheng, R., Ho-Baillie, A., Huang, S., Chen, S., Wen, X., Hao, X., Green, M.A., 2015. Methylammonium lead bromide perovskite-based solar cells by vapor-assisted deposition. *J. Phys. Chem. C* 119 (7), 3545–3549.
- Stoumpos, C.C., Mao, L., Malliakas, C.D., Kanatzidis, M.G., 2017. Structure-band gap relationships in hexagonal polytypes and low-dimensional structures of hybrid tin iodide perovskites. *Inorg. Chem.* 56 (1), 56–73.
- Stranks, S.D., Eperon, G.E., Grancini, G., Menelaou, C., Alcocer, M.J.P., Leijtens, T., Herz, L.M., Petrozza, A., Snaith, H.J., 2013. Electron-hole diffusion lengths exceeding 1 micrometer in an organometal trihalide perovskite absorber. *Science* 342 (6156), 341.
- Suzuki, A., Taguchi, M., Oku, T., Okita, M., Minami, S., Fukunishi, S., Tachikawa, T., 2021. Additive effects of methyl ammonium bromide or formamidinium bromide in methylammonium lead iodide perovskite solar cells using decaphenylcyclopentasilane. *J. Mater. Sci. Mater. Electron.* 32 (22), 26449–26464.
- Vega, E., Mollar, M., Marf, B., 2018. Effect of guanidinium on the optical properties and structure of the methylammonium lead halide perovskite. *J. Alloy. Compd.* 739, 1059–1064.
- Xu, H., Liang, Z., Ye, J., Xu, S., Wang, Z., Zhu, L., Chen, X., Xiao, Z., Pan, X., Liu, G., 2022. Guanidinium-assisted crystallization modulation and reduction of open-circuit voltage deficit for efficient planar FAPbBr₃ perovskite solar cells. *Chem. Eng. J.* 437, 135181.
- Yerramilli, A.S., Chen, Y., Alford, T.L., 2021. Passivation of triple cation perovskites using guanidinium iodide in inverted solar cells for improved open-circuit voltage and stability. *Sustainable Energy Fuels* 5 (9), 2486–2493.
- Zhang, W., Xiong, J., Li, J., Daoud, W.A., 2019. Guanidinium induced phase separated perovskite layer for efficient and highly stable solar cells. *J. Mater. Chem. A* 7 (16), 9486–9496.
- Zhang, W., Xiong, J., Li, J., Daoud, W.A., 2020. Guanidinium passivation for air-stable rubidium-incorporated Cs_(1-x)Rb_xPbI₂Br inorganic perovskite solar cells. *Solar RRL* 4 (6), 2000112.
- Zhao, Y., Zhu, K., 2013. Charge transport and recombination in perovskite (CH₃NH₃)PbI₃ sensitized TiO₂ solar cells. *J. Phys. Chem. Lett.* 4 (17), 2880–2884.